

Analytic Spectral Integration of Birefringence-Induced Iridescence

S. Steinberg 



Figure 1: (Left) Photo captured through the window of a train using a common handheld device and viewed through the polarising lens of a pair of sunglasses. The window exhibits stress-induced birefringence which gives rise to the visible iridescence. Notice that the visual effect is most powerful when the incident light is reflected off the road as light reflected around the Brewster's angle is strongly polarized. (Right) An optically anisotropic slab rendered using our method and exhibiting iridescence induced by birefringence as well. Incident light was assumed to be partially polarized.

Abstract

Optical phenomena that are only observable in optically anisotropic materials are generally ignored in the computer graphics. However, such optical effects are not restricted to exotic materials and can also be observed with common translucent objects when optical anisotropy is induced, e.g. via mechanical stress. Furthermore accurate prediction and reproduction of those optical effects has important practical applications. We provide a short but complete analysis of the relevant electromagnetic theory of light propagation in optically anisotropic media and derive the full set of formulations required to render birefringent materials. We then present a novel method for spectral integration of refraction and reflection in an anisotropic slab. Our approach allows fast and robust rendering of birefringence-induced iridescence in a physically faithful manner and is applicable to both real-time and offline rendering.

CCS Concepts

• *Computing methodologies* → *Rendering*; • *Applied computing* → *Physics*;

1. Introduction

An optically transmissive media is called anisotropic when its optical properties, as perceived by a light wave, vary based on the light wave's polarization and propagation direction within the media. This distinction causes waves with different polarization orientation to take different paths within the medium, an effect called *birefringence* — also known as “double refraction”. Birefringence gives rise to unique optical phenomena unseen in isotropic materials and admits a vast collection of practical applications, such as light modulators used in liquid crystal displays (LCD), tools in

medical diagnosis and stress analysis. Optical anisotropy can arise naturally, like in crystals due to the anisotropic electrical properties of the molecules that compose their lattices, and can also be induced artificially by a variety of mechanisms, most notably via *photoelasticity* — common transparent materials, like glass and plastic, become birefringent under mechanical deformation which changes their physical properties (see figures 1, 2). Light refracting through such matter produces interference between the emerging light waves causing *iridescence*, which is a colour change that depends on viewing angle. Iridescence can also be observed in

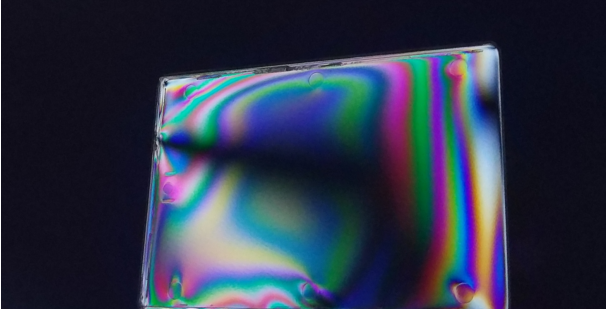


Figure 2: Birefringence-induced iridescence due to deformations under non-uniform mechanical stress (photoelasticity) causing varying fringe patterns: A simple plastic card was placed between an *s*-polarized light source and a polarization filter, which amplifies the perceived iridescence. The dark path where no iridescence is visible coincides with the principal axis of the anisotropic material and is a unique visual property of iridescence that arises due to optical anisotropy.

isotropic materials, as a result of diffraction effects due to the microscopic structure of the material or due to interactions with a thin-film. However, unlike the isotropic case, birefringence-induced iridescence does not require physical structures at a scale smaller than the light's coherence area and can arise with simple optically anisotropic objects at scales that are orders of magnitude greater.

The interesting properties of optical anisotropy come at a cost of a relatively more complicated underlying theory and introduce mechanics which are less intuitive, e.g. the well known law of reflection and Snell's law of refraction no longer apply, instead a reflection or refraction splits the incident wave into a couple of outgoing waves whose directions and amplitudes depend on the incidence angle and polarization. Furthermore, the visual effects induced by optical anisotropy are most prominent when viewed through a polarization filter and otherwise generally do not produce a dramatic change in material appearance. This has caused the computer graphics community to overall ignore optical anisotropy, with a few exceptions. Nonetheless, our interest in reproducing the visual response of birefringence-induced iridescence is twofold: First, it can be perceived in common objects that admit birefringence, like gemstones or moulded plastics, especially, but not only, when viewed through a polarization filter like sun-glasses' lenses, and second, predicting the interference patterns generated due to photoelasticity is of great practical interest as there is direct relation between the stress tensor and the induced birefringence (see figure 2).

To simplify our discussion we consider only homogeneous uniaxial anisotropic media and focus on physically accurate reproduction of birefringence-induced iridescence in the case of reflection off and refraction through a perfectly smooth, infinite slab. The rest of the paper is structured as follows: We cover related work, in the realm of computer graphics as well as optics, in the following section. Then, in section 3, we provide an overview of the relevant electromagnetic theory and derive directly from Maxwell's equations the equations for the normal modes, electric fields and Poynting vectors for an electromagnetic wave propagating through an optically anisotropic medium, as well as the equations for the Fres-

nel coefficients. Birefringence-induced iridescence is discussed in section 4 where we obtain a closed-form formulation of the amplitudes of a coherent wave ensemble that reflects off or refracts through an anisotropic slab. In section 5 we discuss the challenges of rendering iridescence and present our analytic spectral integration approximation. We evaluate the presented method and discuss limitations and future work in section 6, and conclude in section 7.

2. Related Work

Work that considers birefringency in the field of computer graphics is scarce and is mostly limited to rendering double refraction or reproducing the appearance of gemstones. [WW08] and [TTW94] deal solely with polarization aware rendering of double refractions in ray traced renderers. Likewise [LSG12] aims to render double refractions of biaxial media by pre-computing a lookup table. A framework for the rendering of faceted gemstones is presented by [GS04] and remains the state-of-the-art work in modelling gemstones. A novel approach for depth imaging [BGK16] places a birefringent crystal in front of a camera lens and considers the geometry induced by the double refraction.

On the other hand, there is a rich body of work in optics literature that deals with light propagation in optically anisotropic media. [Yeh79] and [Blo61] are a cornerstone of modern crystallography and deal with the theoretical foundations of optical anisotropy and its applications in experimental optics. Attempts to derive formulations for geometric tracing of rays in an anisotropic media generally employ one of two methods – Electromagnetic wave theory or Huygens principle. Of the earliest work to use the former method [Sim83] calculates the extraordinary wave's phase velocities from which the normal modes and ray directional cosines are deduced. Follow-up work employ similar methods and present simpler analytic methods [Lia90; Zha92]. The continuity of tangential component of the wave vector across media interfaces was used by [Lek91] to provide explicit vector formulations for the ray directions and Fresnel coefficients of isotropic and anisotropic boundaries. An iterative numerical approach to calculate the directional cosines of the extraordinary ray is developed by [MHC93]. Huygens himself was one of the first to discuss birefringency [Huy07] and the pioneering work [Sta62; AS02] that employs Huygens wavelets to derive the ray directions in anisotropic media places severe restrictions on the orientation of the optic axis relative to the incidence plane. Further work relaxes the constraints [ASyG02] and deals with internal reflections [AR16]. However, it is not until recently that the equivalence between methods that use the electromagnetic wave theory and Huygens principle was formally shown [Wan18a]. Additional relevant work employs Fermat's principle [Wan18b] to derive ray directions and considers absorption in conductive crystals [WLXW08].

We also consider computer graphics work that aims to reproduce the appearance of iridescence outside the realm of anisotropic optics. Similar to our method, [SM92] pre-integrates the integrals of the cosine of the phase shift over the support of the colour matching functions. The most notable work is [BB17] where an analytic expression for spectral integration of the phase shifts generated by reflections off a dielectric or conducting base layer covered by a thin-film of varying thickness is provided, and upon which

the initial steps of our spectral integration method are based on. A general purpose framework for modelling diffractions is described by [CHB*12] where adjacent patches of the microscopic structure are analysed. Iridescence which results from nano-scale biological structures that cause diffraction is considered by [Sad08], who purposes a multi-layered model of thin-films to render iridescent butterfly wings but does not discuss spectral integration. A data driven approach is presented by [DTS*14] where pre-integrated look-up tables are generated to allow real-time rendering. Additional wave-optics related work focuses on rendering glints [JHY*14], modelling scratches in materials [RGB16; WVJH17; VWH18] and rendering diffractions that result from arbitrary micro-scale structures in conductors and other materials [YHW*18].

3. Background

While there has been extensive study of optical anisotropy, as well as light propagation in such media (see [BW99; YY03] for an in-depth analysis), we feel that an easy-to-understand overview, aimed at an audience outside the realm of physics, is lacking. Therefore, in our supplemental material we provide a short but complete overview that discusses the relevant electromagnetic theory and derives the formulations for the electric fields and Poynting vectors for electromagnetic waves propagating in an optically anisotropic medium directly from Maxwell's equations. In this section we list the results without going into detail.

Optical anisotropy is the property where light perceives a different refractive index based on its polarization and propagation direction in an anisotropic medium. For simplicity we limit our discussion to *uniaxial* materials, i.e. anisotropic materials that give rise to two refractive indices, an *ordinary* and an *extraordinary* indices-of-refraction, η_o and η_e , and a single distinguished direction, the *optic axis*, denoted as $A = [\alpha, \beta, \gamma]^T$. We consider two homogeneous and magnetically isotropic adjacent media with their interface forming the XZ -plane in our coordinate system of choice and $I_i = [0, \cos\theta, \sin\theta]^T$ being a ray propagating from the source medium ($Y > 0$) to the destination medium ($Y < 0$) with the incidence point being at the origin (see figure 3). The incidence angle of I_i is then θ and we denote η_i as the effective index-of-refraction as perceived by the incident wave propagating in the source medium, which for isotropic materials is simply the refractive index of the source medium.

We denote $\mathbf{E} = e^{i(qy - Kz - \omega t)} [\mathbf{E}_x, \mathbf{E}_y, \mathbf{E}_z]^T$ as the electric field vector, with ω being the angular frequency and K , the *incidence parameter*, which is the tangential component of the incident wave vector:

$$K = \eta_i \sin(\theta) \quad (1)$$

q , the *normal mode*, is the component of the wave's propagation direction that is normal to the surface, and differs between ordinary and extraordinary rays:

$$q_o^\pm = \pm \sqrt{\hat{\epsilon}_o - K^2}$$

$$q_e^\pm = \frac{\pm \sqrt{\hat{\epsilon}_o} \sqrt{\hat{\epsilon}_e (\beta^2 \Delta\epsilon + \hat{\epsilon}_o) + K^2 (\alpha^2 \Delta\epsilon - \hat{\epsilon}_e) + \beta \gamma K \Delta\epsilon}}{\hat{\epsilon}_o + \beta^2 \Delta\epsilon} \quad (2)$$

where $\Delta\epsilon = \hat{\epsilon}_e - \hat{\epsilon}_o$ and $\hat{\epsilon}_{o,e} = \eta_{o,e}^2$.

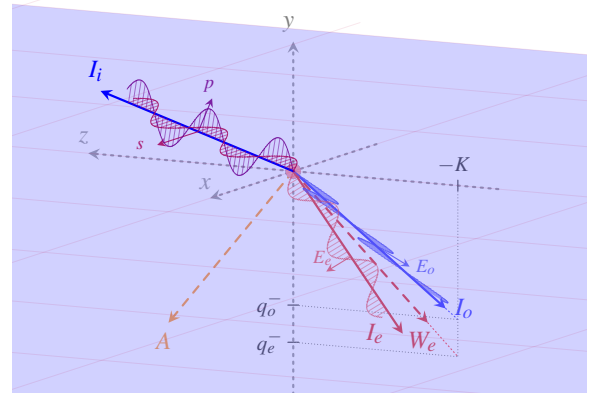


Figure 3: Randomly polarized light wave, incident to an anisotropic material, refracted into linearly-polarized ordinary and extraordinary rays. Note that the extraordinary Poynting vector leaves the plane of incidence (YZ) and is detached from its wave's direction of propagation. The incident parameter K and the normal modes q_o^-, q_e^- for the (un-normalized) ordinary and extraordinary waves are marked. The incidence parameter remains constant across surface boundaries for all participating waves.

As q is the wave vector's normal component, normal modes superscripted with a plus correspond to waves travelling upwards while normal modes with a minus correspond to waves travelling downwards, in other words q^+ correspond to reflections and q^- to refractions. The electric fields \mathbf{E} are then given by:

$$\mathbf{E}_o^\pm = \frac{1}{N_o^\pm} [-\beta K - \gamma q_o^\pm, \alpha K, \alpha q_o^\pm]^T$$

$$\mathbf{E}_e^\pm = \frac{1}{N_e^\pm} \begin{bmatrix} \alpha \hat{\epsilon}_o \\ \beta \hat{\epsilon}_o + q_e^\pm (\gamma K - \beta q_e^\pm) \\ \gamma \hat{\epsilon}_o - K (\gamma K - \beta q_e^\pm) \end{bmatrix} \quad (3)$$

where N are normalization factors. Finally the ray direction, or *Poynting vector*, for a given normal mode and incidence parameter, is simply

$$\mathbf{I} = \frac{1}{N} \mathbf{E} \times (\mathbf{W} \times \mathbf{E}) \quad (4)$$

where $\mathbf{W} = [0, q, -K]^T$ is the wave's direction of propagation.

An important theoretical conclusion is that the incidence parameter K remains constant for all participating waves, the effective refractive index perceived by a wave propagating in an anisotropic media is then

$$\eta_{ef} = \frac{K}{\sin\phi} = \sqrt{q^2 + K^2} \quad (5)$$

where ϕ is the wave's angle of refraction or reflection. And indeed while for ordinary waves η_{ef} remains fixed at η_o , extraordinary waves perceive a refractive index between η_o and η_e . We define the *maximal incidence parameter* as

$$K_e^{max} = \eta_e \sqrt{\frac{\eta_o^2 + \beta^2 \Delta\epsilon}{\eta_e^2 - \gamma^2 \Delta\epsilon}} \quad K_o^{max} = \eta_o \quad (6)$$

When $K \geq K_e^{max}$ total-reflection occurs: The refracted wave be-

comes evanescent and its associated Poynting vector is complex and parallel to the surface interface.

Note that the indices-of-refraction generally vary with the wave's frequency, temperature and other factors, therefore can be treated as constants only for a given monochromatic wave. For succinctness we ignore dispersion and will only discuss it briefly in section 5. Likewise, to keep the discussion as simple as possible, we ignore conductive media and therefore assume real indices-of-refraction and neglect absorption. However, conductivity in the context of anisotropic media is discussed in our supplemental material and would be trivial to incorporate into our model.

Fresnel coefficients We also require the Fresnel transmission and reflection coefficients for the interfaces between isotropic and anisotropic media. We derive the equations in our supplemental material and the formulas for the Fresnel coefficients for isotropic-to-anisotropic and anisotropic-to-isotropic interfaces are listed in full in appendix A.

4. Birefringence-Induced Iridescence

Iridescence, which is colour variations that occur on certain surfaces depending on light incident angle, wavelength and view angle, occurs due to wave interference induced by the phase shifts that result from different paths taken by a light wave. While iridescence also appears in isotropic media, in the anisotropic case unique complexities and properties arise. Due to the nature of an optically anisotropic medium, which alters the polarization state of light refracting through it, it is imperative to take polarization into account even if we were to assume random polarization of the incident light wave. To compose polarized waves of equal wavelength we use *Jones vectors*, which are two-dimensional complex-valued vectors that describe coherent light:

$$J = \begin{bmatrix} J_s \\ J_p \end{bmatrix} = \begin{bmatrix} E_s e^{i\psi_s} \\ E_p e^{i\psi_p} \end{bmatrix} e^{i(qy - Kz - \omega t)} \quad (7)$$

where ψ_s and ψ_p are the waves' phases, E_s and E_p are the peak scalar amplitudes and \mathbf{W} is the wave's direction of propagation. We define the implied reference frame as the orthogonal directions of s- and p-polarization, that is J_s and J_p describe orthogonal waves and the amplitude of the composed wave, defined as the magnitude of the Jones vector, is trivially deduced via the Pythagorean theorem:

$$|J| = \sqrt{J_s J_s^* + J_p J_p^*} = \sqrt{E_s^2 + E_p^2} \quad (8)$$

The power carried by the Jones vector is then simply the magnitude squared $|J|^2 = E_s^2 + E_p^2$. Composed orthogonal waves can not interfere, therefore constructive-destructive wave interference is restricted to superposed waves in each orthogonal component, J_s and J_p , separately. Interference effects are then twofold – 1. Colour variations due to the phase shifts of superposed waves in each component of the orthogonal frame; and 2. change of the polarization state as a result of the non-uniform magnitude change in each of the components. While the former is visible with the naked eye, the latter generally requires a polarizing filter to observe.

We study the case of refraction through an infinite XZ -plane parallel homogeneous anisotropic slab of uniform thickness d (see figure 4a), with indices of refraction η_o , η_e and optic axis A . For sim-

licity we assume a planar incident wave, which simplifies the geometric deductions of the optical path differences. In that setting notice an obvious but crucial observation:

Lemma 4.1 A given incident ray, parameterized by its incidence parameter K , gives rise to up to four distinct ray directions inside a homogeneous plane parallel anisotropic slab of constant thickness: An ordinary and an extraordinary ray propagating downwards and an ordinary and an extraordinary ray propagating upwards.

Proof As we saw in section 3 the incidence parameter K , wave's normal component q and the medium constants uniquely define a ray travelling through an anisotropic medium. The incidence parameter remains constant across interface boundaries (equation 5) and for that given incidence parameter there are up to four distinct waves propagating through the anisotropic medium, therefore the only possible ray directions are the Poynting vectors associated with the normal modes q_o^- , q_e^- for downward rays and q_o^+ , q_e^+ for upwards rays. \square

Therefore, given a planar wave with incidence parameter K propagating in the upper medium, which admits the refractive index η_i , and incident at angle θ to the anisotropic slab, we define I_o , I_e as the ordinary and extraordinary ray directions propagating downwards in the slab and t_o , t_e as the Fresnel transmission coefficients of refraction into ordinary and extraordinary rays, respectively. \hat{t}_{os} , \hat{t}_{op} , \hat{t}_{es} and \hat{t}_{ep} are the Fresnel transmission coefficients for ordinary and extraordinary rays, respectively, refracting from the slab into the lower medium as s- and p-polarized waves. Furthermore \hat{t}_o , \hat{t}_e are defined as the ordinary and extraordinary ray directions propagating upwards in the slab, and r_{oo} , r_{oe} , r_{eo} , r_{ee} are the Fresnel reflection coefficients for slab internal reflections at the upper interface ($y \equiv 0$) for the respective rays and \hat{r}_{oo} , \hat{r}_{oe} , \hat{r}_{eo} , \hat{r}_{ee} are, similarly, the Fresnel reflection coefficients at the lower interface ($y \equiv -d$). The Poynting vectors are computed via equation 4 while the Fresnel coefficients are computed via the respective equations in appendix A.

To compute phase shifts we need to examine the optical path difference between two light paths. We define the *primary path* to be the order 1 path (no internal reflections) which refracts into the slab as an ordinary ray and exits the slab at the point $O = [0, -d, 0]$ (marked in blue in figure 4a), while a *secondary path* is any other path that starts by refracting into the slab and escapes downwards from the slab at point O . The *order* of a path, n , is defined as the count of internal double-reflections.

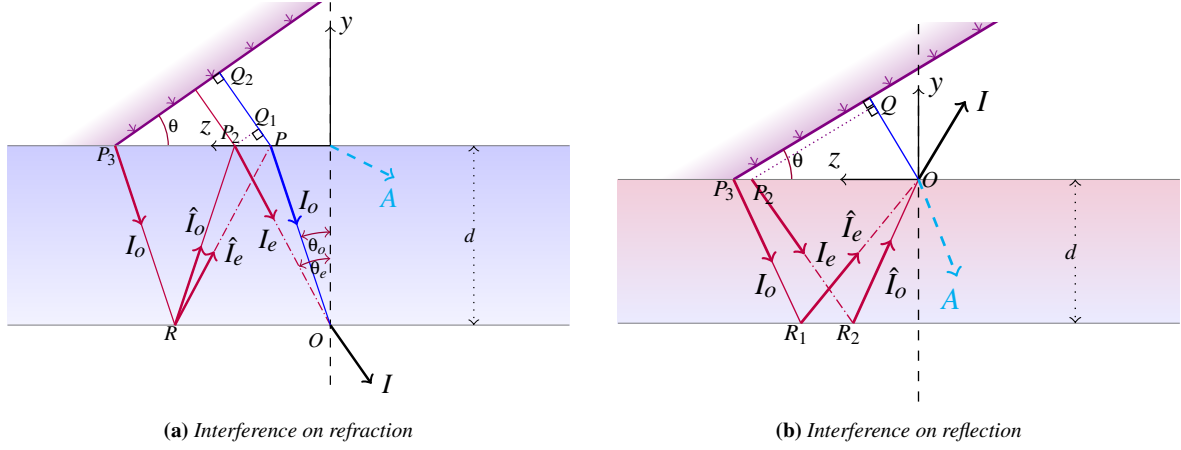
The *optical path length* $OPL(l, \eta)$ of a light path is defined as

$$OPL(l, \eta) = l\eta \quad (9)$$

with l being the path length and η the refractive index. The refractive indices as perceived by the extraordinary rays are the effective refractive indices computed via equation 5. Given \mathcal{P} , an OPL of a secondary path, the optical path difference (OPD) between the primary and a secondary path is

$$\Delta\mathcal{P} = \mathcal{P} - a\eta_i - OPD_o \quad (10)$$

where $OPD_o = |PO|\eta_o$ is the OPL of the primary path inside the slab (which is constant for a given K and does not depend on the secondary path), a is the length of the primary path taken by the



(a) Interference on refraction

(b) Interference on reflection

Figure 4: An incident planar wavefront (marked by a solid violet line with arrows indicating the direction of propagation), with angle of incidence θ , is refracted into the slab and some of the possible paths taken by the light are pictured (marked in purple). The primary path is marked in blue. Solid paths are ordinary rays while dash-dotted paths are extraordinary rays. The different paths result in different optical lengths inducing interference once the rays become superposed on (left) refraction through the slab or (right) reflection off the slab, with the exit ray I marked by a solid black arrow. E.g. the optical path difference between the optical path lengths of the order 1 path Q_2PO and the order 2 path P_3RP_2O (on the left image) results in a phase shift once the light is refracted out of the slab in direction I .

incident wavefront outside the slab and depends on the secondary path (e.g. $a = |Q_1P|$ in figure 4a when the secondary path starts at P_2 , or $a = |Q_2P|$ when the secondary path starts at P_3). Given the z -value of the entry point of the secondary path (that is, the point where the secondary path refracts into the slab), a becomes:

$$a(z) = |z - P_z| \sin \theta \quad (11)$$

where P_z is the z component of P , the entry point of the primary path. It is easy to see that this holds also when the secondary path's entry point does not reside on the incidence plane (the YZ -plane), which can happen as extraordinary paths generally leave the plane of incidence, that is a only depends on the z value of the entry point. The phase difference induced by the OPD is $\Delta\phi = k\Delta\mathcal{P}$ with $k = \frac{2\pi}{\lambda}$ being the wavenumber and λ the wavelength, the resulting phase shift is then $e^{i\Delta\phi}$. Therefore the amplitude of a secondary path is

$$Z = t_1 r t_2 e^{i\Delta\phi} e^{i(qy - Kz - \omega t)} \quad (12)$$

where t_1 and t_2 are the relevant Fresnel transmission coefficients for refraction into and out of the slab and \mathbf{r} is the product of reflection coefficients accounting for all internal reflections. Remember that \mathbf{r} can be complex when reflections introduce a phase shift.

We denote the Jones vector \mathcal{J}_n as the aggregate amplitudes of all path of order n refracting through the slab. We aggregate paths using linear operators, in the form of 2×2 matrices, where the amplitudes corresponding to paths that begin with an ordinary ray reside in row 1, while paths that end with an ordinary ray reside in column 1. Row 2 and column 2 are used for paths that begin or end with an extraordinary ray, respectively. Then, the amplitudes for $n = 0$ are:

$$D_0 = \begin{bmatrix} e^{ik\Delta\mathcal{P}_o^\downarrow} & 0 \\ 0 & e^{ik\Delta\mathcal{P}_e^\downarrow} \end{bmatrix} \quad (13)$$

where $\Delta\mathcal{P}_o^\downarrow$ and $\Delta\mathcal{P}_e^\downarrow$ are the OPDs for order 0 ordinary and extraordinary paths, respectively, with \downarrow superscript indicating rays

that propagate downwards in the slab. Using D_0 we now can write the Jones vector for $n = 0$:

$$\mathcal{J}_0 = \begin{bmatrix} t_o \\ t_e \end{bmatrix}^T D_0 \begin{bmatrix} \hat{i}_{os} & \hat{i}_{op} \\ \hat{i}_{es} & \hat{i}_{ep} \end{bmatrix} e^{i(qy - Kz - \omega t)} \quad (14)$$

The OPD (equations 10, 11) of a path is a piece-wise sum of the OPL and z -displacement of each step the path takes. Then, we define the linear operator \mathcal{D}^\downarrow , which, when acting upon a Jones vector, describes how the ordinary and extraordinary rays propagate downwards from the top interface through the slab, and reflect at the bottom interface. Analogously, the linear operator \mathcal{D}^\uparrow propagates the energy from the bottom interface and reflects at the top interface:

$$\mathcal{D}^\downarrow = \begin{bmatrix} \hat{r}_{oo} e^{ik\Delta\mathcal{P}_o^\downarrow} & \hat{r}_{oe} e^{ik\Delta\mathcal{P}_o^\downarrow} \\ \hat{r}_{eo} e^{ik\Delta\mathcal{P}_e^\downarrow} & \hat{r}_{ee} e^{ik\Delta\mathcal{P}_e^\downarrow} \end{bmatrix} \quad \mathcal{D}^\uparrow = \begin{bmatrix} \hat{r}_{oo} e^{ik\Delta\mathcal{P}_o^\uparrow} & \hat{r}_{oe} e^{ik\Delta\mathcal{P}_o^\uparrow} \\ \hat{r}_{eo} e^{ik\Delta\mathcal{P}_e^\uparrow} & \hat{r}_{ee} e^{ik\Delta\mathcal{P}_e^\uparrow} \end{bmatrix} \quad (15)$$

Then, just as D_0 describes the amplitudes of the order 0 paths, $\mathcal{D}^\downarrow \mathcal{D}^\uparrow D_0$ describes the aggregated amplitudes of all order 1 paths, and for succinctness the operator $\mathcal{D} = \mathcal{D}^\downarrow \mathcal{D}^\uparrow$ is defined. See appendix B for explicit equations for \mathcal{D} and for all the OPDs involved.

The aggregated amplitudes of the 2^{2n+1} paths of order n is then simply $D_0 \mathcal{D}^n$ and the corresponding Jones vector is

$$\mathcal{J}_n = \begin{bmatrix} t_o \\ t_e \end{bmatrix}^T \mathcal{D}^n D_0 \begin{bmatrix} \hat{i}_{os} & \hat{i}_{op} \\ \hat{i}_{es} & \hat{i}_{ep} \end{bmatrix} e^{i(qy - Kz - \omega t)} \quad (16)$$

Due to the energy conservation of the Fresnel reflection coefficients it holds that $|\mathcal{D}| \leq 1$. As the equality can only happen under total-reflection, we can assume $|\mathcal{D}| < 1$ and therefore can apply the well known sum of a geometric series $I + M + M^2 + \dots = (I - M)^{-1}$ (trivially proven by multiplying both sides by $I - M$) to write the

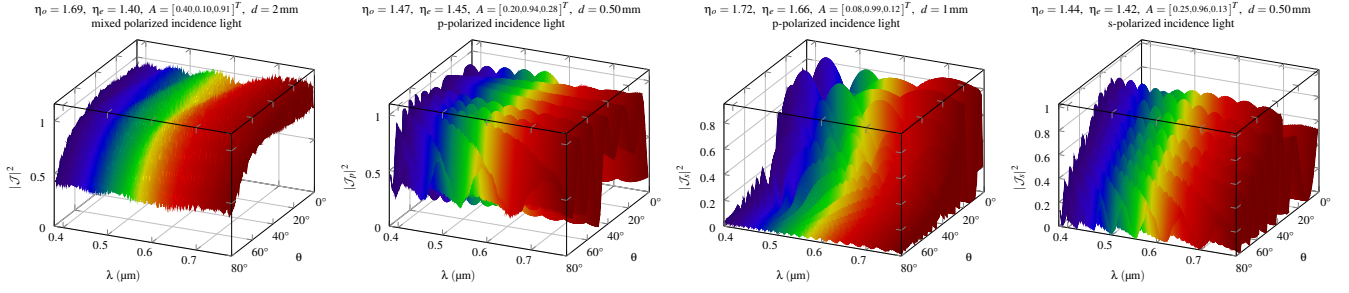


Figure 5: Plots of the magnitude of the Jones vector \mathcal{J} or its linearly-polarized components \mathcal{J}_s , \mathcal{J}_p for a variety of material constants for the case of refraction through an anisotropic slab. The perceived index-of-refraction of the incidence wave propagating in the source medium is assumed to be $\eta_i = 1$ and the incidence polarization is assumed to be random. While interference is generally subtle, at some angles and material constants unique patterns emerge.

closed-form expression for the aggregated amplitudes of all paths refracting through an anisotropic slab:

$$\mathcal{J} = \sum_{n=0}^{\infty} \mathcal{J}_n = \begin{bmatrix} \hat{t}_o \\ \hat{t}_e \end{bmatrix}^T (I - \mathcal{D})^{-1} D_0 \begin{bmatrix} \hat{t}_{os} & \hat{t}_{op} \\ \hat{t}_{es} & \hat{t}_{ep} \end{bmatrix} e^{i(qy - Kz - \omega t)} \quad (17)$$

Reflection and transmission power ratios As discussed in the supplemental material the power ratios that define the surface transmissivity and reflectivity do not generally equal the absolute value squared of the Fresnel coefficients. However, assuming an (isotropic) surrounding medium with constant index-of-refraction, we can neglect accounting for the power ratios of the singular transmissions and reflections because the angle of incidence to the slab and angle of refraction or reflection out of the slab are always equal as is the impedance. And indeed one can check that when computing the power ratio of refraction through the slab or reflection out of the slab (using the power ratio equations in the supplemental material), all the terms except the Fresnel coefficients cancel out. If, in the case of refraction, the source medium ($y > 0$) and destination medium ($y < -d$) have different material constants then \mathcal{J} should be modulated by the appropriate power ratio.

Iridescence when reflecting off an anisotropic slab Iridescence can be introduced on reflection off an anisotropic slab in a manner mostly similar to the case of refraction (see figure 4b). We go over the differences and list the full formulas for \mathcal{D} and \mathcal{J} for the case of reflection in our supplemental material.

5. Rendering photoelasticity

Iridescence arises due to the changes in magnitude of $\mathcal{J} = \sum_n \mathcal{J}_n$ as function of wavelength, therefore to render iridescent effects it is required to integrate that function over the visible spectrum. The spectral integration can be done numerically – at fixed sample points or stochastically, or analytically if an analytic solution exists. Spectral renderers that perform stochastic (e.g Monte Carlo) integration of the visible spectrum could use the closed-form expression of \mathcal{J} (equation 17) directly, while traditional renderers that employ a limited set of spectral bands (typically RGB for tristimulus renderers) are required to perform spectral integration. Unfortunately finding an analytic solution to the spectral integral of the

closed-form expression for \mathcal{J} is not straightforward, and calculating numerically requires a prohibitively high sample count in order to avoid spectral aliasing that arises due to the high frequency of the integrand (see figure 6b and section 6), which makes the spectral integration a challenging task for real-time and even offline renderers.

5.1. Spectral Integration

Spectral integration transforms a wavelength spectrum into discrete spectral bands using *spectral sensitivity functions* $\Lambda_j(\lambda)$. For tristimulus renderers the sensitivity functions would usually be the CIE XYZ colour matching functions, commonly designated $\bar{x}(\lambda)$, $\bar{y}(\lambda)$ and $\bar{z}(\lambda)$ (see figure 6a), however in general any number of spectral bands can be used. To express outbound radiance ($\text{Wsr}^{-1}\text{m}^{-2}$) we assume that Λ is normalized across the visible spectrum, that is

$$\int_{\lambda} \Lambda(\lambda) d\lambda = 1$$

We first focus on the case of refraction through an anisotropic slab however the approach is similar for reflection. Let \mathcal{S} be the spectral integration operator defined as $\mathcal{S}(f, \Lambda) = \int_{\lambda} \Lambda(\lambda) f(\lambda) d\lambda$ where f is an integrable function of wavelength and Λ is a spectral sensitivity function. Given \mathcal{J} , due to the way we defined the magnitude of a Jones vector (equation 8) the spectral integration can be done on each component separately:

$$\begin{aligned} \mathcal{S}(|\mathcal{J}|^2, \Lambda) &= \int_{\lambda} \Lambda(\lambda) (|\mathcal{J}_s|^2 + |\mathcal{J}_p|^2) d\lambda = \\ &= \mathcal{S}(|\mathcal{J}_s|^2, \Lambda) + \mathcal{S}(|\mathcal{J}_p|^2, \Lambda) \end{aligned} \quad (18)$$

For simplicity we assume that the Fresnel coefficients as well as the phase shifts induced by the OPDs are independent of the wavelength, therefore the only dependence on wavelength arises in the $k = \frac{2\pi}{\lambda}$ factor in the exponents. This assumption hampers our ability to faithfully model some materials, like dispersive dielectrics, that exhibit strong variance in their permittivity as a function of wavelength. However, as spectral integration is done separately for each spectral sensitivity function, that can be partially mitigated by choosing a representative index-of-refraction for each spectral band, and potentially integrating over more bands.

We focus first on the s-polarized component of the Jones vectors

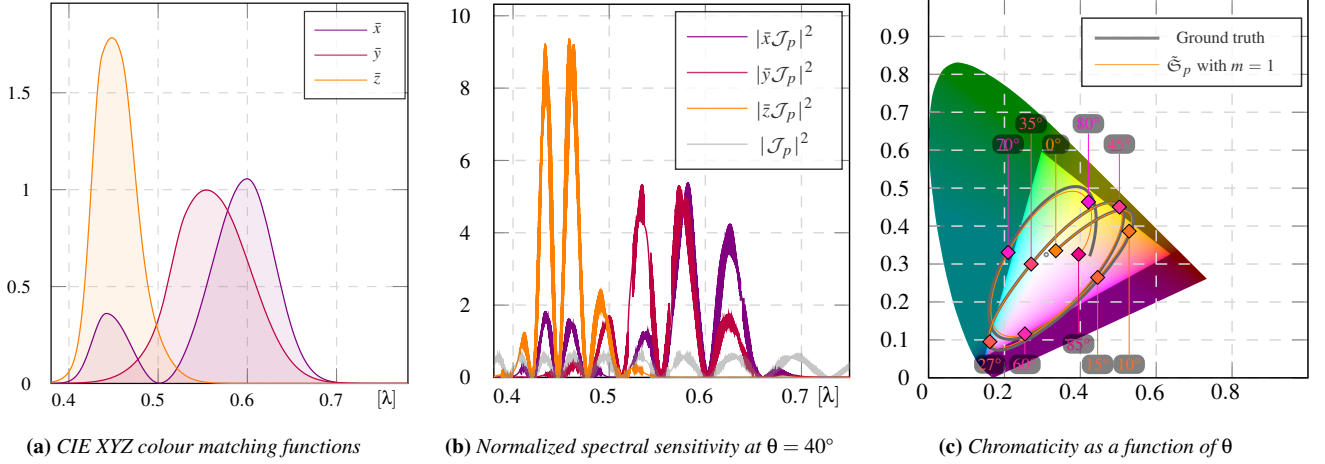


Figure 6: Spectral integration of a given $|\mathcal{J}_p|^2$, the intensity of refracted s -polarized light as a function of wavelength, over the support of normalized spectral sensitivity functions, which are (a) the CIE XYZ colour matching functions. (b) The primary difficulty arises in efficiently and accurately approximating the spectral integrals due to the high frequency integrands. (c) The plotted chromaticity of the spectral integrals as a function of incidence angle θ . The thick black line plots the ground truth obtained by numerically integrating the spectral integral of our closed-form expression, $\mathcal{S}(|\mathcal{J}_p|^2, \Lambda)$ while the thin orange line is our approximation, $\tilde{\mathcal{S}}_p$ with $m = 1$. The approximation matches the ground truth perfectly except at grazing angles. To amplify the effects of interference a fully s -polarized incident wave was used.

and for brevity denote $J_n = (\mathcal{J}_n)_s$. J_n is then a sum of electric field amplitudes of the form of equation 12, i.e $J_n = \sum_p^{2n+1} E_p e^{i\Delta\phi_p}$ with $\Delta\phi_p$ and E_p being the phase shift and the wavelength independent scalar electric field amplitudes, respectively. Then we can write the spectral integral as (see appendix C):

$$\begin{aligned} \mathcal{S} \left(\left| \sum_n J_n \right|^2, \Lambda \right) &= \\ &= \sum_j E_j^2 + 2 \sum_{l=1}^{\infty} E_j E_{j+l} \int_{\lambda} \Lambda(\lambda) \cos(\Delta\phi_j - \Delta\phi_{j+l}) d\lambda \end{aligned} \quad (19)$$

The first term, $\mathcal{E} = \sum_{j=0}^{\infty} E_j^2$, is the sum of transmitted energy of all possible paths refracting through the slab. It can be computed in closed-form if we take the component-wise complex magnitude squared of \mathcal{D}^\downarrow and \mathcal{D}^\uparrow (equation 15), and write their sum as

$$\bar{\mathcal{D}} = \begin{bmatrix} |\hat{r}_{oo}|^2 |r_{oo}|^2 + |\hat{r}_{oe}|^2 |r_{eo}|^2 & |\hat{r}_{oo}|^2 |r_{oe}|^2 + |\hat{r}_{oe}|^2 |r_{ee}|^2 \\ |\hat{r}_{eo}|^2 |r_{oo}|^2 + |\hat{r}_{ee}|^2 |r_{eo}|^2 & |\hat{r}_{eo}|^2 |r_{oe}|^2 + |\hat{r}_{ee}|^2 |r_{ee}|^2 \end{bmatrix} \quad (20)$$

then the transmitted energy becomes

$$\mathcal{E} = \begin{bmatrix} t_o^2 \\ t_e^2 \end{bmatrix}^T (I - \bar{\mathcal{D}})^{-1} \begin{bmatrix} r_{os}^2 \\ r_{es}^2 \end{bmatrix} \quad (21)$$

where we used the fact that the component-wise complex magnitude of D_0 (equation 13) is simply the identity matrix. The second term, which we denote $2\mathcal{H}$, is a double sum that iterates over the phase differences of all pairs of paths. While \mathcal{E} is essentially wavelength agnostic, \mathcal{H} is the term that is responsible for the wave interference effects and is more difficult to compute. We focus the remainder of this section on approximating \mathcal{H} .

Let $Z_{n+l} = t_\xi |\mathbf{r}_n| |\mathbf{r}_l| e^{i\Delta\phi_n} e^{i\Delta\phi_l} \hat{t}_{\zeta s} e^{i(qy - Kz - \omega t)}$ (equation 12) be the amplitude of an order $n + l$ path composed of an order l path

segment on top of a order n base path. And let the amplitude of the order n path be $Z_n = t_\xi |\mathbf{r}_n| e^{i\Delta\phi_n} \hat{t}_{\zeta s} e^{i(qy - Kz - \omega t)}$. The subscripts $\xi, \zeta, \chi \in \{o, e\}$ denote the type of ray the paths start and end with, the products of internal reflections coefficients for the base path and final segment are $|\mathbf{r}_n|$ and $|\mathbf{r}_l|$, respectively, and the phase shifts are $e^{i\Delta\phi_n}$ and $e^{i\Delta\phi_l}$. We denote the scalar electric fields of Z_n and Z_{n+l} as $E_n = |Z_n|$ and $E_{n+l} = |Z_{n+l}|$, then

$$\begin{aligned} E_n E_{n+l} &= t_\xi^2 |\mathbf{r}_n|^2 |\mathbf{r}_l| \hat{t}_{\zeta s} \hat{t}_{\chi s} \\ \cos(\Delta\phi_n - \Delta\phi_{n+l}) &= \cos(\Delta\phi_l) \end{aligned} \quad (22)$$

that is, $\cos(\Delta\phi_n - \Delta\phi_{n+l})$ is independent of $\Delta\phi_n$, the base path's phase. Therefore, we can approximate \mathcal{H} by only accounting for the pairs where one path is a "descendant" of the other, in which case the inner sum in \mathcal{H} becomes independent of the outer sum. As discussed in section 4, $|\mathbf{r}_l| e^{i\Delta\phi_l}$ is a product of a sequence of l factors each one of the additive factors in \mathcal{D} , therefore applying equations 22 to equation 19 results in the following expression for $\tilde{\mathcal{H}} \approx \mathcal{H}$:

$$\tilde{\mathcal{H}} = \mathcal{S}(H_0, \Lambda) + \begin{bmatrix} t_o^2 \\ t_e^2 \end{bmatrix}^T (I - \bar{\mathcal{D}})^{-1} T_s \sum_{l=1}^{\infty} \mathcal{S}(\Re(\mathcal{D}^l), \Lambda) \begin{bmatrix} \hat{t}_{os} \\ \hat{t}_{es} \end{bmatrix} \quad (23)$$

where \Re is the real part and T_s is

$$T_s = \begin{bmatrix} \hat{t}_{os} & 0 \\ 0 & \hat{t}_{es} \end{bmatrix}$$

the term H_0 is the most significant term of \mathcal{H} , the interference between the two order 0 paths, which is otherwise not captured by our approximation:

$$H_0 = t_o \hat{t}_{os} t_e \hat{t}_{es} \cos(k\Delta\mathcal{P}_o^\downarrow - k\Delta\mathcal{P}_e^\downarrow) \quad (24)$$

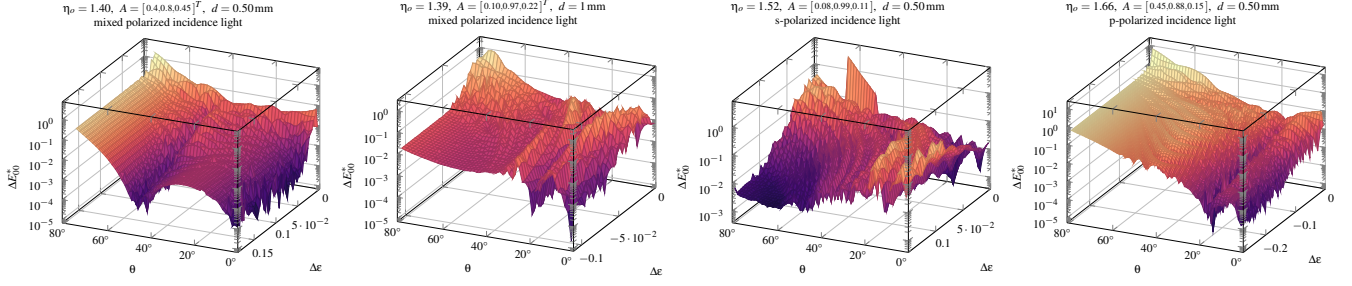


Figure 7: Plots of the chromaticity deviations, expressed via the CIE DE2000 [SWD05] colour difference formula (values of less than 1 are considered imperceptible colour difference), between the approximation $\tilde{\mathcal{S}}$ and numerical integrations of the closed-form solution, $\mathcal{S}(|\mathcal{J}|^2, \Lambda)$, as functions of incidence angle θ and the material's birefringence, $\Delta\epsilon$, for a variety of material constants.

and we use the fact that $|z| \cos(\text{Arg}(z)) = \Re(z)$, for any $z \in \mathbb{C}$ where $\text{Arg}()$ is the complex argument.

The spectral integral (equation 19) can now be written as follows

$$\mathcal{S}\left(\left|\sum_n J_n\right|^2, \Lambda\right) \approx \mathcal{E} + 2\tilde{\mathcal{H}} \quad (25)$$

The results for the p-polarized component of \mathcal{J}_n is identical except \hat{t}_{os} and \hat{t}_{es} are replaced with \hat{t}_{op} and \hat{t}_{ep} , respectively, in \mathcal{E} and $\tilde{\mathcal{H}}$ (equations 21 and 23).

5.2. Implementation and Practical Considerations

To render birefringence-induced iridescence we need to evaluate equation 25, the approximated spectral integral, at each rendered sample point. \mathcal{E} is given in closed-form via equation 21 however no closed-form solution was found for $\tilde{\mathcal{H}}$. To evaluate $\tilde{\mathcal{H}}$ we choose m , a maximum value for the summation index l in equation 23, and expand the expressions \mathcal{D}^l to rewrite the sum as a 2x2 matrix whose elements are sums of expressions of the form $E \cos(k\Delta\mathcal{P})$, where E is independent of the phase shift. As m is constant this can be done offline. Evaluating $\tilde{\mathcal{H}}$ reduces then to evaluating the spectral integrals $\mathcal{S}(\cos(k\Delta\mathcal{P}), \Lambda)$. To that end we employ curve fitted analytic approximations for \bar{x} , \bar{y} , \bar{z} , the CIE XYZ colour matching functions [WSS13], to precompute $\mathcal{S}(\cos(k\Delta\mathcal{P}), \bar{x})$, $\mathcal{S}(\cos(k\Delta\mathcal{P}), \bar{y})$ and $\mathcal{S}(\cos(k\Delta\mathcal{P}), \bar{z})$ into a 1D look-up table parameterized by the OPD $\Delta\mathcal{P}$.

The expanded expression for \mathcal{D}^l is potentially a 2x2 matrix where each element is a sum consisting of 2^l elements. In practice, however, setting $m = 1$ provides very accurate results (except at grazing angles, i.e. when $\theta > 70^\circ$) and choosing a higher value for m significantly increases cost of computation while doing little to reduce the error as the error stems from the approximation's bias: It only accounts for some of phase differences, ignoring the others. See section 6 for numeric and visual evaluation of our method. We assume $m = 1$ for the rest of the paper and rewrite equation 25 as

$$\begin{aligned} \tilde{\mathcal{S}}_s = & \begin{bmatrix} \hat{t}_o^2 \\ \hat{t}_e^2 \end{bmatrix}^T (I - \bar{\mathcal{D}})^{-1} \left[\begin{bmatrix} \hat{t}_{os}^2 \\ \hat{t}_{es}^2 \end{bmatrix} + 2T_s \cdot \mathcal{S}(\Re(\mathcal{D}), \Lambda) \begin{bmatrix} \hat{t}_{os} \\ \hat{t}_{es} \end{bmatrix} \right] + \\ & + 2\mathcal{S}(H_0, \Lambda) \end{aligned} \quad (26)$$

with $\tilde{\mathcal{S}} = [\tilde{\mathcal{S}}_s, \tilde{\mathcal{S}}_p]^T$ being the approximation for the spectral integral, that is $\tilde{\mathcal{S}}_s \approx \mathcal{S}(|\mathcal{J}_s|^2, \Lambda)$.

Given an anisotropic slab, its material constants and an incident ray our rendering pipeline is implemented as follows:

1. Compute the normal modes and electric fields (equations 2, 3), the Poynting vectors $I_o, \hat{I}_o, I_e, \hat{I}_e$ (equation 4) and the appropriate Fresnel coefficients for reflections and refractions (appendix A).
2. Compute the OPDs $\Delta\mathcal{P}_o^\downarrow, \Delta\mathcal{P}_e^\downarrow, \Delta\mathcal{P}_o^\uparrow, \Delta\mathcal{P}_e^\uparrow$ and using those evaluate the spectral integrals of $\mathcal{S}(H_0, \Lambda)$ and $\mathcal{S}(\Re(\mathcal{D}), \Lambda)$, for $\Lambda \in \{\bar{x}, \bar{y}, \bar{z}\}$. In practice this requires a total of five queries to the precomputed table.
3. Compute the spectral integrals $\mathcal{S}(|\mathcal{J}|^2, \Lambda)$, for each colour band, using the approximation $\tilde{\mathcal{S}}$, detailed in equation 26.

Total-reflection should be considered as well, that is when $K \geq K^{max}$ (equation 6) for the upper or lower interface. See our supplemental material for an example implementation.

6. Discussion and Evaluation

Our primary contributions are equations 25 and 26, the approximate forms for the spectral integral of $|\mathcal{J}|^2$, which enable efficient and accurate rendering of birefringence-induced iridescence. Our solution is simple to integrate into common tristimulus real-time and offline renderers, as well as spectral renderers. Some spectral renderers that perform stochastic multiple importance sampling [WND*14] or a variation would require special handling, e.g. generation of spectral sensitivity functions on the fly, however this is beyond the scope of this paper.

We evaluate our method based on the radiometric precision of the approximation $\tilde{\mathcal{S}}$. To that end we numerically integrate our closed-form expression for \mathcal{J} (equation 17) and employ it as the ground truth. We first compare numerically by examining the differences between the approximation $\tilde{\mathcal{S}}$ and the ground truth expressed via the CIE DE2000 metric ΔE_{00}^* as function of incidence angle for a variety of material constants (see figure 7).

Furthermore, we rendered anisotropic slabs with a variety of material constants under different lighting conditions and polarization filters. Rendering using the analytic approximation $\tilde{\mathcal{S}}$ was performed as outlined in section 5. For evaluation we also rendered

identical scenes by numerically integrating the spectral integrals of \mathcal{J} with 3 spectral samples, taken at the peaks of the tristimulus spectral sensitivity functions – 450 nm, 550 nm and 600 nm for the CIE XYZ colour matching functions, as well as 8, 32, 128, 512 and 2048 spectral samples uniformly distributed between 380 nm and 700 nm. Strongly birefringent materials, especially at grazing angles or thicker slabs, may exhibit visible spectral aliasing even with 2048 spectral samples, therefore a ground truth was rendered using 16384 samples (51 samples per nanometre). The CIE XYZ colour matching functions \bar{x} , \bar{y} , \bar{z} were used and the final results were transformed to sRGB colour space. The analytic approximation renderings were compared against their numerically integrated counterparts and images of their colour difference can be seen in figure 9. Largely $\tilde{\mathcal{E}}$ approximates the major iridescence bands as well as the total energy transmitted through the anisotropic slab in an essentially indistinguishable fashion from the ground truth (generally $\Delta E_{00}^* \leq 1$). The greatest errors ($\Delta E_{00}^* < 4$) can be seen around the minor iridescence bands (see figure 9a) which are poorly captured by the approximation. Likewise, depending on view orientation a weak colour shift of the entire slab can be seen that is slightly more pronounced in the ground truth ($\Delta E_{00}^* \in [1, 2]$) than the analytic approximation. The inaccuracies are mostly due to the loss of information in the approximation and it is unlikely that higher approximation orders ($m > 1$) would avail in alleviating those small errors.

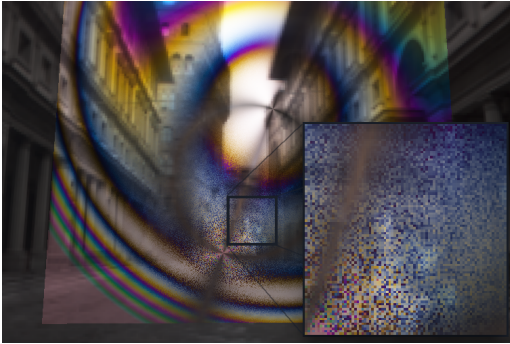


Figure 8: Certain birefringent materials can admit strong aliasing artefacts as the spectral integral, $\tilde{\mathcal{E}}$, is sampled at discrete values of θ , the incident angle. This is especially visible at regions of strong iridescence when viewed under a cross polarizer.

Optical coherence We have assumed fully coherent light propagating inside an anisotropic slab, however physical light sources are not point lights and have a finite extent. This means that the region, around any point in space and time where the light waves that form the ensemble remain correlated, and therefore *coherent*, is finite [MW95]. As coherency diminishes so does the ability of the ensemble to superpose and produce interference effects. For our method to be physically correct, we need to ensure that it is applied within the *region of coherence*. Rigorous formulation of optical coherency is beyond the scope of this paper, however we notice that, in practice, coherency is generally maintained with slabs that produce visible iridescence. For example, consider the slab that exhibits strong birefringence depicted in figure 9c. The coherence size of sunlight reaching earth is up to $60 \mu\text{m}$ [MGFG12] (inversely

proportional to the solid angle subtended by the source) while the spatial offset between the order 1 ordinary and extraordinary paths in said 0.50 mm slab is less than $10 \mu\text{m}$ (for $\theta = \frac{\pi}{2}$).

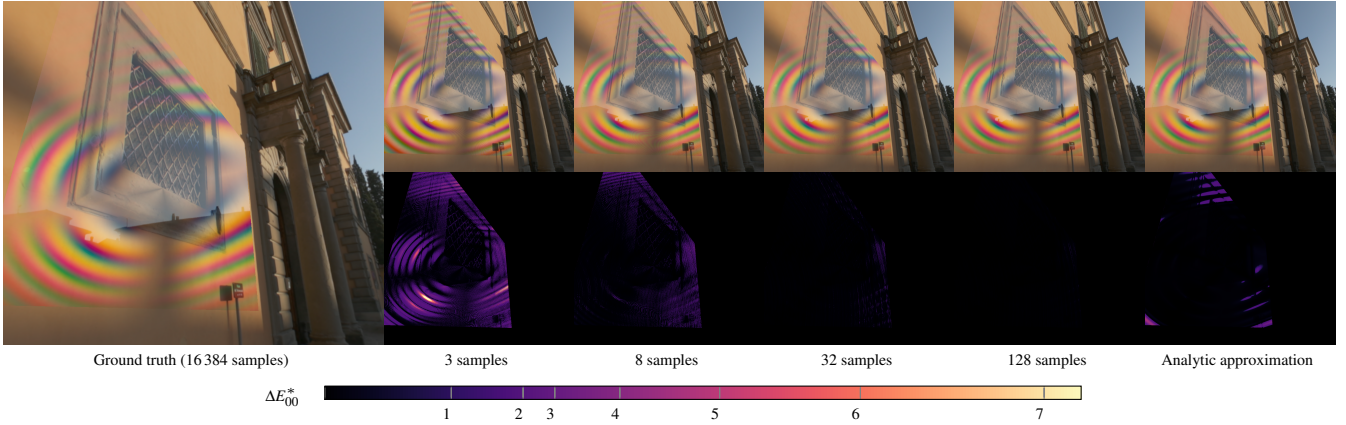
Spatial aliasing As discussed in section 4 and can be seen in figure 5 the integrand \mathcal{J} can oscillate with very high frequency. Just as this results in spectral aliasing when numerically integrating, this can also result in spatial aliasing as can be seen in figure 8, with identical patterns ($\Delta E_{00}^* < 1$) reproducible with the ground truth as well. A brute force solution would be to increase the sample count (e.g. by super-sampling), however this is costly and would not fully alleviate the problem. Note that the Fresnel coefficients, and in turn \mathcal{D} , are “well-behaved”, that is they admit a vastly lower Nyquist rate than the OPDs (see supplemental material). The Nyquist rate of $\tilde{\mathcal{E}}$ (equation 26) is, therefore, dominated by the phase shifts in \mathcal{D} and H_0 (equations 15 and 24). Spatial anti-aliasing of the spectral integrals $\mathcal{S}(\mathcal{R}(\mathcal{D}))$ and $\mathcal{S}(H_0)$ would therefore be a robust solution and the development of this approach is left for future work.

Spectral integration method	Frame time	
Analytic approximation	1.09	ms
<i>Numeric integration</i>		
3 spectral samples	1.30	ms
8 spectral samples	1.73	ms
32 spectral samples	3.84	ms
128 spectral samples	12.20	ms
512 spectral samples	45.50	ms
2048 spectral samples	0.20	sec
<i>Ground truth</i>		
16384 spectral samples	2.00	sec

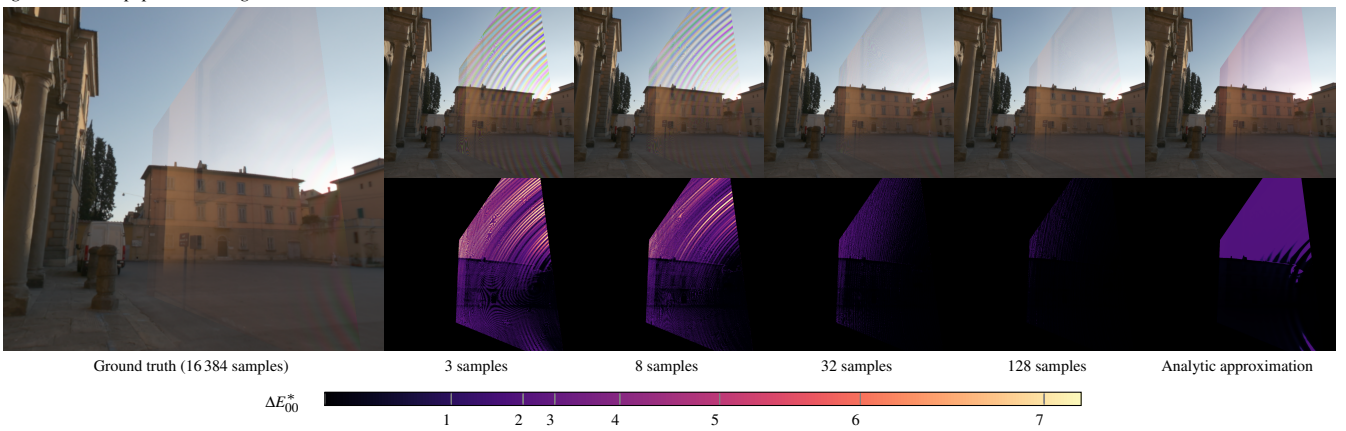
Table 1: Performance comparison of spectral integration methods for rendering birefringence-induced iridescence. Rendering was done at 1920×1080 resolution on a mobile NVIDIA™ GeForce™ 1070. For numerical integration the visible range was assumed to be 380 nm to 700 nm. Dispersion was ignored and permittivity was assumed to be constant across the entire visible spectrum.

Performance As discussed in section 5, rendering birefringence-induced iridescence using the developed analytic approximation requires computing the electric fields, Poynting vectors, the Fresnel coefficients and finally evaluating $\tilde{\mathcal{E}}$ which consists of five look-ups to the precomputed spectral integration table. While the heavy arithmetics can be cumbersome on low-powered hardware, this is still easily within the capabilities of modern hardware and can be rendered at real-time frame rates even on integrated graphics accelerators.

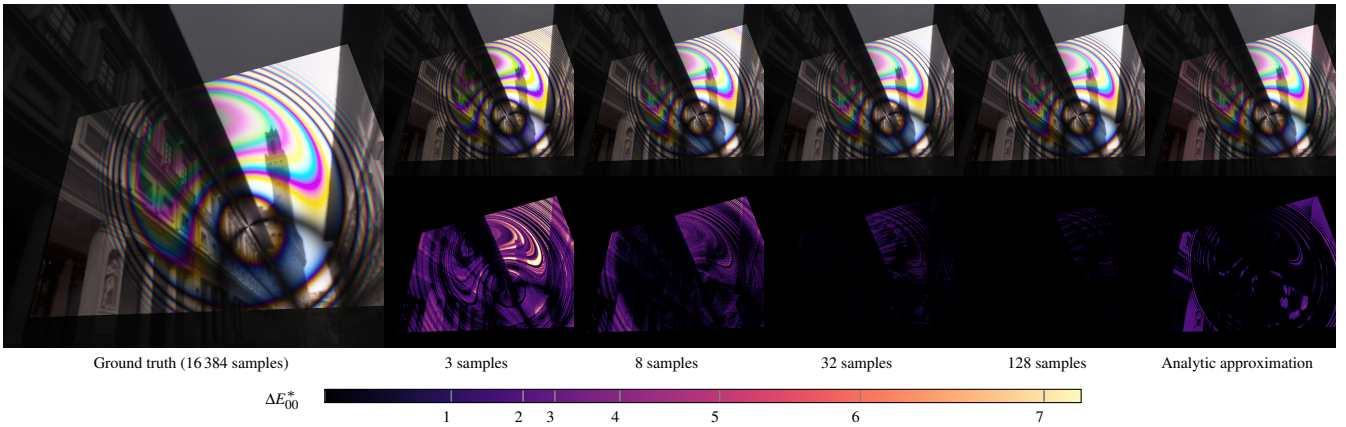
To evaluate the performance of the analytic approximation the scene seen in figure 9a was rendered using a common consumer-grade graphics accelerator, a mobile NVIDIA™ GeForce™ 1070. The measured frame times are listed in table 1. The primary cost in the case of the analytic approximation arises in computing the Poynting vectors and the Fresnel coefficients, while the numeric integration cost is dominated by the complex arithmetics in equation 17, nonetheless we did not focus on performance and no optimizations were performed.



(a) A weakly birefringent slab with $\eta_o = 1.40$, $\eta_e = 1.38$, $A = [-0.54, 0.80, 0.27]^T$ and $d = 1.25$ mm. Incident light was assumed to consist of 75% s-polarized light and 25% p-polarized light.



(b) A birefringent slab with $\eta_o = 1.50$, $\eta_e = 1.51$, $A = [0.25, 0.97, 0.00]^T$ and $d = 3.50$ mm rendered at an angle where little iridescence is visible. Incident light was assumed to be mixed polarized. Notice that spectral aliasing is clearly visible even with 128 spectral samples.



(c) A strongly birefringent slab with $\eta_o = 1.775$, $\eta_e = 1.231$, $A = [0.084, 0.979, -0.187]^T$ and $d = 1.15$ mm. Incident light was assumed to be virtually fully p-polarized and an s-polarization filter was used. The cross polarization causes the background to appear very dark while amplifying iridescence.

Figure 9: Rendering of birefringence-induced iridescence at various settings and material constants using our analytic approximation, $\tilde{\mathcal{S}}$, compared against numerically integrating the spectral integral $\mathcal{S}(|\mathcal{T}|^2, \Lambda)$ with different count of spectral samples. The ground truth was rendered using 16384 samples. For a quantifiable comparison of accuracy the CIE DE2000 metric was used and the difference map (compared with the ground truth) is shown below each image. Severe coloured ringing artefacts appear when rendered at less than 32 samples for thin slabs, while thin grey ringing artefacts are visible with a higher sample count. Notice that compared to the ground truth our analytic approximation fails to fully capture the minor coloured bands as well as the very slight colour shift of the entire slab.

Limitations and future work Our discussion is centred on smooth, homogeneous, optically anisotropic uniaxial slabs and our results are restricted to this setting. A common scenario that we would like to model is an isotropic material, like glass, becoming birefringent when subject to mechanical stress, in which case the material constants, the optic axis and dielectric constants, vary across the material and especially around any discontinuities in the material. While we can simulate the stress distribution by altering the material constants at each sampled point in the rendered image, our discussion still assumes homogeneity and therefore the optic axis and dielectric constants remain constant across all the paths traced through the slab at each sample point. This effectively restricts our approximation to slabs where the material constants do not vary significantly across its thickness. Relaxing our method to non-homogeneous media would make it more applicable to a variety of practical considerations and, therefore, warrants further attention in future work.

We also assumed perfectly smooth surfaces and while that assumption is reasonable for crystals it is of interest to consider more sophisticated bidirectional reflectance and transmittance functions in our model.

Finally, we ignored dispersive effects during the spectral integration process by electing to use a representative permittivity, and in turn fixed ray directions and Fresnel coefficients, for each spectral band. This makes sense as the indices-of-refraction generally vary slowly and very smoothly over the visible spectrum, furthermore the discretization of the permittivity does not give rise to aliasing artefacts, unlike numeric integration with discrete spectral samples where even thousands of samples can produce visible artefacts with thick slabs and at grazing angles. Nonetheless, it is of interest to design a method for robust spectral integration in dispersive media.

7. Conclusion

A method for the reproduction of iridescence that arises due to birefringence in an optically anisotropic uniaxial slab was demonstrated. Our method is faithfully derived from the underlying optical theory and the presented analytic approximation of the spectral integral works with an arbitrary optic axis and material constants and is suitable for use in real-time and offline renderers.

Furthermore, we derived a simple, closed-form expression for the aggregated amplitudes of all the light paths that occur as a planar wave refracts into an anisotropic slab, and used it as a ground truth to rigorously validate the radiometric accuracy of our method. The results are mostly virtually indistinguishable from the ground truth, and we believe that our work has practical applications inside and outside the realm of computer graphics.

References

- [AR16] ALEMÁN-CASTAÑEDA, LUIS A. and ROSETE-AGUILAR, MARTHA. "Reflection formulae for ray tracing in uniaxial anisotropic media using Huygens's principle". *J. Opt. Soc. Am. A* 33.11 (Nov. 2016), 2198–2205. DOI: [10.1364/JOSAA.33.002198](https://doi.org/10.1364/JOSAA.33.002198). URL: <http://josaa.osa.org/abstract.cfm?URI=josaa-33-11-2198>.
- [AS02] AVENDAÑO-ALEJO, MAXIMINO and STAVROUDIS, ORESTES N. "Huygens's principle and rays in uniaxial anisotropic media. II. Crystal axis orientation arbitrary". *J. Opt. Soc. Am. A* 19.8 (Aug. 2002), 1674–1679. DOI: [10.1364/JOSAA.19.001674](https://doi.org/10.1364/JOSAA.19.001674). URL: <http://josaa.osa.org/abstract.cfm?URI=josaa-19-8-1674>.
- [ASyG02] AVENDAÑO-ALEJO, MAXIMINO, STAVROUDIS, ORESTES N., and y GOITIA, ANA ROSA BOYAIN. "Huygens's principle and rays in uniaxial anisotropic media. I. Crystal axis normal to refracting surface". *J. Opt. Soc. Am. A* 19.8 (Aug. 2002), 1668–1673. DOI: [10.1364/JOSAA.19.001668](https://doi.org/10.1364/JOSAA.19.001668). URL: <http://josaa.osa.org/abstract.cfm?URI=josaa-19-8-1668>.
- [BB17] BELCOUR, LAURENT and BARLA, PASCAL. "A Practical Extension to Microfacet Theory for the Modeling of Varying Iridescence". *ACM Trans. Graph.* 36.4 (July 2017), 65:1–65:14. ISSN: 0730-0301. DOI: [10.1145/3072959.3073620](https://doi.org/10.1145/3072959.3073620). URL: <http://doi.acm.org/10.1145/3072959.3073620>.
- [BGK16] BAEK, SEUNG-HWAN, GUTIERREZ, DIEGO, and KIM, MIN H. "Birefractive Stereo Imaging for Single-shot Depth Acquisition". *ACM Trans. Graph.* 35.6 (Nov. 2016), 194:1–194:11. ISSN: 0730-0301. DOI: [10.1145/2980179.2980221](https://doi.org/10.1145/2980179.2980221). URL: <http://doi.acm.org/10.1145/2980179.2980221>.
- [Blo61] BLOSS, F. DONALD. *An introduction to the methods of optical crystallography / F. Donald Bloss*. English. Saunders College Philadelphia, 1961. ISBN: 0030102200 2.
- [BW99] BORN, M. and WOLF, E. *Principles of Optics*. Cambridge University Press, Oct. 1999, 952. ISBN: 978-0521642224 3.
- [CHB*12] CUYPERS, TOM, HABER, TOM, BEKAERT, PHILIPPE, et al. "Reflectance Model for Diffraction". *ACM Trans. Graph.* 31.5 (Sept. 2012), 122:1–122:11. ISSN: 0730-0301. DOI: [10.1145/2231816.2231820](https://doi.org/10.1145/2231816.2231820).
- [DTS*14] DHILLON, D. S., TEYSSIER, J., SINGLE, M., et al. "Interactive Diffraction from Biological Nanostructures". *Computer Graphics Forum* 33.8 (2014), 177–188. DOI: [10.1111/cgf.12425](https://doi.org/10.1111/cgf.12425). eprint: <https://onlinelibrary.wiley.com/doi/pdf/10.1111/cgf.12425>. URL: <https://onlinelibrary.wiley.com/doi/abs/10.1111/cgf.12425>.
- [GS04] GUY, STEPHANE and SOLER, CYRIL. "Graphics Gems Revisited: Fast and Physically-based Rendering of Gemstones". *ACM Trans. Graph.* 23.3 (Aug. 2004), 231–238. ISSN: 0730-0301. DOI: [10.1145/1015706.1015708](https://doi.org/10.1145/1015706.1015708). URL: <http://doi.acm.org/10.1145/1015706.1015708>.
- [Huy07] HUYGENS, C. *Treatise on Light*. Echo Library, 2007. ISBN: 9781406813753. URL: <https://books.google.se/books?id=Xq5EjJlgV6gC2>.
- [JHY*14] JAKOB, WENZEL, HAAN, MILO, YAN, LING-QI, et al. "Discrete Stochastic Microfacet Models". *ACM Trans. Graph.* 33.4 (July 2014), 115:1–115:10. ISSN: 0730-0301. DOI: [10.1145/2601097.2601186](https://doi.org/10.1145/2601097.2601186). URL: <http://doi.acm.org/10.1145/2601097.2601186>.
- [Lek91] LEKNER, J. "Reflection and refraction by uniaxial crystals". *Journal of Physics Condensed Matter* 3 (Aug. 1991), 6121–6133. DOI: [10.1088/0953-8984/3/32/017](https://doi.org/10.1088/0953-8984/3/32/017).
- [Lia90] LIANG, QUAN-TING. "Simple ray tracing formulas for uniaxial optical crystals". *Appl. Opt.* 29.7 (Mar. 1990), 1008–1010. DOI: [10.1364/AO.29.001008](https://doi.org/10.1364/AO.29.001008). URL: <http://ao.osa.org/abstract.cfm?URI=ao-29-7-1008>.
- [LSG12] LATORRE, PEDRO, SERON, FRANCISCO J., and GUTIERREZ, DIEGO. "Birefringence: calculation of refracted ray paths in biaxial crystals". *The Visual Computer* 28.4 (Apr. 2012), 341–356. ISSN: 1432-2315. DOI: [10.1007/s00371-011-0619-2](https://doi.org/10.1007/s00371-011-0619-2). URL: <https://doi.org/10.1007/s00371-011-0619-2>.
- [MGFG12] MASHAAL, HEYLAL, GOLDSTEIN, ALEX, FEUERMAN, DANIEL, and GORDON, JEFFREY M. "First direct measurement of the spatial coherence of sunlight". *Opt. Lett.* 37.17 (Sept. 2012), 3516–3518. DOI: [10.1364/OL.37.003516](https://doi.org/10.1364/OL.37.003516).

- [MHC93] McCLAIN, STEPHEN C., HILLMAN, LLOYD W., and CHIPMAN, RUSSELL A. "Polarization ray tracing in anisotropic optically active media. II. Theory and physics". *J. Opt. Soc. Am. A* 10.11 (Nov. 1993), 2383–2393. DOI: [10.1364/JOSAA.10.002383](https://doi.org/10.1364/JOSAA.10.002383). URL: <http://josaa.osa.org/abstract.cfm?URI=josaa-10-11-2383>.
- [MW95] MANDEL, L. and WOLF, E. *Optical Coherence and Quantum Optics*. Sept. 1995, 1192–9.
- [RGB16] RAYMOND, BORIS, GUENNEBAUD, GAËL, and BARLA, PASCAL. "Multi-scale Rendering of Scratched Materials Using a Structured SV-BRDF Model". *ACM Trans. Graph.* 35.4 (July 2016), 57:1–57:11. ISSN: 0730-0301. DOI: [10.1145/2897824.2925945](https://doi.org/10.1145/2897824.2925945). URL: <http://doi.acm.org/10.1145/2897824.2925945>.
- [Sad08] SADEGHI, IMAN. "A physically based anisotropic iridescence model for rendering morpho butterflies photo-realistically". In *Proc. of Iridescence: More Than Meets the Eye*. 2008, 11–3.
- [Sim83] SIMON, MARIA C. "Ray tracing formulas for monoaxial optical components". *Appl. Opt.* 22.2 (Jan. 1983), 354–360. DOI: [10.1364/AO.22.000354](https://doi.org/10.1364/AO.22.000354). URL: <http://ao.osa.org/abstract.cfm?URI=ao-22-2-354>.
- [SM92] SMITS, BRIAN E. and MEYER, GARY W. "Newton's Colors: Simulating Interference Phenomena in Realistic Image Synthesis". *Photorealism in Computer Graphics*. Ed. by BOUATOUCH, KADI and BOUVILLE, CHRISTIAN. Berlin, Heidelberg: Springer Berlin Heidelberg, 1992, 185–194. ISBN: 978-3-662-09287-3. DOI: [10.1007/978-3-662-09287-3_13](https://doi.org/10.1007/978-3-662-09287-3_13). URL: https://doi.org/10.1007/978-3-662-09287-3_13.
- [Sta62] STAVROUDIS, ORESTES N. "Ray-Tracing Formulas for Uniaxial Crystals". *J. Opt. Soc. Am.* 52.2 (Feb. 1962), 187–191. DOI: [10.1364/JOSA.52.000187](https://doi.org/10.1364/JOSA.52.000187). URL: <http://www.osapublishing.org/abstract.cfm?URI=josa-52-2-187>.
- [SWD05] SHARMA, GAURAV, WU, WENCHENG, and DALAL, EDUL N. "The CIEDE2000 color-difference formula: Implementation notes, supplementary test data, and mathematical observations". *Color Research & Application* 30.1 (2005), 21–30. DOI: [10.1002/col.20070](https://doi.org/10.1002/col.20070). eprint: <https://onlinelibrary.wiley.com/doi/pdf/10.1002/col.20070>. URL: <https://onlinelibrary.wiley.com/doi/abs/10.1002/col.20070>.
- [TTW94] TANNENBAUM, DAVID C., TANNENBAUM, PETER, and WOZNY, MICHAEL J. "Polarization and Birefringency Considerations in Rendering". *Proceedings of the 21st Annual Conference on Computer Graphics and Interactive Techniques*. SIGGRAPH '94. New York, NY, USA: ACM, 1994, 221–222. ISBN: 0-89791-667-0. DOI: [10.1145/192161.192204](https://doi.org/10.1145/192161.192204).
- [VWH18] VELINOV, ZDRAVKO, WERNER, SEBASTIAN, and HULLIN, MATTHIAS B. *Real-Time Rendering of Wave-Optical Effects on Scratched Surfaces*. 2018–3.
- [Wan18a] WANG, PENGQIAN. "Geometrical ray tracing in uniaxial crystals: direct formulas and the equivalence between the electromagnetic wave method and Huygens' principle". *J. Opt. Soc. Am. A* 35.7 (July 2018). DOI: [10.1364/JOSAA.35.001114](https://doi.org/10.1364/JOSAA.35.001114). URL: <http://josaa.osa.org/abstract.cfm?URI=josaa-35-7-1114>.
- [Wan18b] WANG, PENGQIAN. "Ray refraction in uniaxial crystals by Fermat's principle". *Appl. Opt.* 57.18 (June 2018), 4950–4954. DOI: [10.1364/AO.57.004950](https://doi.org/10.1364/AO.57.004950). URL: <http://ao.osa.org/abstract.cfm?URI=ao-57-18-4950>.
- [WLXW08] WANG, YANYANG, LIANG, LIANG, XIN, HONG, and WU, LEI. "Complex ray tracing in uniaxial absorbing media". *J. Opt. Soc. Am. A* 25.3 (Mar. 2008), 653–657. DOI: [10.1364/JOSAA.25.000653](https://doi.org/10.1364/JOSAA.25.000653). URL: <http://josaa.osa.org/abstract.cfm?URI=josaa-25-3-653>.
- [WND*14] WILKIE, ALEXANDER, NAWAZ, SEHARA, DROSKE, MARC, et al. "Hero Wavelength Spectral Sampling". *Computer Graphics Forum* 33(4) (*Proceedings of Eurographics Symposium on Rendering 2014*) 33.4 (2014) 8.
- [WSS13] WYMAN, CHRIS, SLOAN, PETER-PIKE, and SHIRLEY, PETER. "Simple analytic approximations to the CIE XYZ color matching functions". <http://jcgf.org/published/0002/02/01/>. 2013, 1–11–8.
- [WVJH17] WERNER, SEBASTIAN, VELINOV, ZDRAVKO, JAKOB, WENZEL, and HULLIN, MATTHIAS B. "Scratch Iridescence: Wave-optical Rendering of Diffractive Surface Structure". *ACM Trans. Graph.* 36.6 (Nov. 2017), 207:1–207:14. ISSN: 0730-0301. DOI: [10.1145/3130800.3130840](https://doi.org/10.1145/3130800.3130840). URL: <http://doi.acm.org/10.1145/3130800.3130840>.
- [WW08] WEIDLICH, ANDREA and WILKIE, ALEXANDER. "Realistic Rendering of Birefringency in Uniaxial Crystals". *ACM Trans. Graph.* 27.1 (Mar. 2008), 6:1–6:12. ISSN: 0730-0301. DOI: [10.1145/1330511.1330517](https://doi.org/10.1145/1330511.1330517). URL: <http://doi.acm.org/10.1145/1330511.1330517>.
- [Yeh79] YEH, POCHI. "Electromagnetic propagation in birefringent layered media". *J. Opt. Soc. Am.* 69.5 (May 1979), 742–756. DOI: [10.1364/JOSA.69.000742](https://doi.org/10.1364/JOSA.69.000742). URL: <http://www.osapublishing.org/abstract.cfm?URI=josa-69-5-742>.
- [YHW*18] YAN, LING-QI, HAAN, MILO, WALTER, BRUCE, et al. "Rendering Specular Microgeometry with Wave Optics". *ACM Trans. Graph.* 37.4 (July 2018), 75:1–75:10. ISSN: 0730-0301. DOI: [10.1145/3197517.3201351](https://doi.org/10.1145/3197517.3201351).
- [YY03] YARIV, AMNON and YEH, POCHI. "Optical waves in crystals: propagation and control of laser radiation". Hoboken, N.J.: John Wiley and Sons, 2003–3.
- [Zha92] ZHANG, WEI-QUAN. "General ray-tracing formulas for crystal". *Appl. Opt.* 31.34 (Dec. 1992), 7328–7331. DOI: [10.1364/AO.31.007328](https://doi.org/10.1364/AO.31.007328). URL: <http://ao.osa.org/abstract.cfm?URI=ao-31-34-7328>.

Appendix A: Fresnel Coefficients

Isotropic-to-Anisotropic Boundary

For the isotropic-to-anisotropic case we look at incident s-polarized and p-polarized waves separately. Then the system of equations for the Fresnel coefficients (see the supplemental material) of an isotropic-to-anisotropic interface given incident s-polarized light becomes:

$$\begin{aligned} \mathbf{E}_I &= e^{i(-q_i y - \omega t)} [-1, 0, 0]^T \\ \mathbf{E}_R &= r_{sp} e^{i(q_i y - \omega t)} [0, \sin \theta, -\cos \theta]^T + r_{ss} e^{i(q_i y - \omega t)} [-1, 0, 0]^T \\ \mathbf{E}_T &= t_{so} e^{i(\hat{q}_o^- y - \omega t)} \hat{\mathbf{E}}_o^- + t_{sp} e^{i(\hat{q}_e^- y - \omega t)} \hat{\mathbf{E}}_e^- \end{aligned} \quad (27)$$

where $q_i = -\eta_i \cos^2 \theta$ where θ is angle of incidence. Similarly the system for incident p-polarized light is:

$$\begin{aligned} \mathbf{E}_I &= e^{i(-q_i y - \omega t)} [0, \sin \theta, \cos \theta]^T \\ \mathbf{E}_R &= r_{pp} e^{i(q_i y - \omega t)} [0, \sin \theta, -\cos \theta]^T + r_{ps} e^{i(q_i y - \omega t)} [-1, 0, 0]^T \\ \mathbf{E}_T &= t_{po} e^{i(\hat{q}_o^- y - \omega t)} \hat{\mathbf{E}}_o^- + t_{pe} e^{i(\hat{q}_e^- y - \omega t)} \hat{\mathbf{E}}_e^- \end{aligned} \quad (28)$$

Solving 27 and 28 results in the following coefficients for an incident p-polarized wave:

$$\begin{aligned} r_{ps} &= \frac{2(\hat{\mathbf{E}}_e^-)_x (\hat{\mathbf{E}}_o^-)_x \cos \theta C_1 (\hat{q}_o^- - \hat{q}_e^-)}{N_1} \\ r_{pp} &= \frac{1}{N_1} \left[-(\hat{\mathbf{E}}_e^-)_x (\hat{\mathbf{E}}_o^-)_z (C_1 - \hat{q}_o^- \cos \theta) (q_i + \hat{q}_e^-) - A_1 (\hat{q}_e^- + q_i) + \right. \\ &\quad \left. + (\hat{\mathbf{E}}_e^-)_z (\hat{\mathbf{E}}_o^-)_x (C_1 - \hat{q}_e^- \cos \theta) (q_i + \hat{q}_o^-) + A_2 (\hat{q}_o^- + q_i) \right] \\ t_{po} &= -2 \frac{(\hat{\mathbf{E}}_e^-)_x \cos \theta (\hat{q}_e^- + q_i) C_1}{N_1} \end{aligned}$$

$$t_{pe} = 2 \frac{(\hat{\mathbf{E}}_o^-)_x \cos \theta (\hat{q}_o^- + q_i) C_1}{N_1} \quad (29)$$

and for an s-polarized wave:

$$\begin{aligned} r_{ss} &= \frac{C_2(q_i - \hat{q}_e^-) + C_3(\hat{q}_o^- - q_i)}{N_1} \\ r_{sp} &= 2q_i \frac{(\hat{\mathbf{E}}_o^-)_z (\hat{\mathbf{E}}_o^-)_y K - (\hat{\mathbf{E}}_o^-)_y (\hat{\mathbf{E}}_o^-)_z K + (\hat{\mathbf{E}}_o^-)_z (\hat{\mathbf{E}}_o^-)_z (\hat{q}_o^- - \hat{q}_e^-)}{N_1} \\ t_{so} &= -2q_i \frac{(\hat{\mathbf{E}}_o^-)_y K \cos \theta + (\hat{\mathbf{E}}_o^-)_z C_1 + (\hat{\mathbf{E}}_o^-)_z \hat{q}_e^- \cos \theta}{N_1} \\ t_{se} &= 2q_i \frac{(\hat{\mathbf{E}}_o^-)_y K \cos \theta + (\hat{\mathbf{E}}_o^-)_z C_1 + (\hat{\mathbf{E}}_o^-)_z \hat{q}_o^- \cos \theta}{N_1} \end{aligned} \quad (30)$$

where

$$\begin{aligned} A_1 &= -(\hat{\mathbf{E}}_e^-)_x (\hat{\mathbf{E}}_o^-)_y K \cos \theta \\ A_2 &= -(\hat{\mathbf{E}}_e^-)_y (\hat{\mathbf{E}}_o^-)_x K \cos \theta \\ C_1 &= q_i \cos \theta - K \sin \theta \\ C_2 &= (\hat{\mathbf{E}}_e^-)_x (\hat{\mathbf{E}}_o^-)_z (C_1 + \hat{q}_o^- \cos \theta) - A_1 \\ C_3 &= (\hat{\mathbf{E}}_e^-)_z (\hat{\mathbf{E}}_o^-)_x (C_1 + \hat{q}_e^- \cos \theta) - A_2 \\ N_1 &= C_2(q_i + \hat{q}_e^-) - C_3(q_i + \hat{q}_o^-) \end{aligned}$$

Anisotropic-to-Isotropic Boundary

The anisotropic-to-isotropic case is handled similarly. The system for Fresnel coefficients in the case of an ordinary wave incident to an anisotropic-to-isotropic interface:

$$\begin{aligned} \mathbf{E}_I &= e^{i(q_o^- y - \omega t)} \mathbf{E}_o^- \\ \mathbf{E}_R &= r_{oo} e^{i(q_o^+ y - \omega t)} \mathbf{E}_o^+ + r_{oe} e^{i(q_e^+ y - \omega t)} \mathbf{E}_e^+ \\ \mathbf{E}_T &= t_{op} e^{i(-q_i y - \omega t)} [0, \sin \theta, \cos \theta]^T + t_{os} e^{i(-q_i y - \omega t)} [-1, 0, 0]^T \end{aligned} \quad (31)$$

and in the case of an extraordinary wave:

$$\begin{aligned} \mathbf{E}_I &= e^{i(q_e^- y - \omega t)} \mathbf{E}_e^- \\ \mathbf{E}_R &= r_{eo} e^{i(q_o^+ y - \omega t)} \mathbf{E}_o^+ + r_{ee} e^{i(q_e^+ y - \omega t)} \mathbf{E}_e^+ \\ \mathbf{E}_T &= t_{ep} e^{i(-q_i y - \omega t)} [0, \sin \theta, \cos \theta]^T + t_{es} e^{i(-q_i y - \omega t)} [-1, 0, 0]^T \end{aligned} \quad (32)$$

Solving 31 and 32 yields the following Fresnel coefficients for an ordinary incident wave:

$$\begin{aligned} r_{oo} &= -\frac{1}{N_2} \left[(\mathbf{E}_e^-)_x (\mathbf{E}_o^-)_z (\hat{q}_o^- - q_e^+) (q_o^+ \cos \phi - D_1) + \right. \\ &\quad \left. + (\mathbf{E}_o^-)_x (\hat{q}_o^- + q_o^+) D_2 + (\mathbf{E}_o^-)_y B_1 - (\mathbf{E}_e^+)_y B_2 \right] \\ r_{oe} &= -\frac{1}{N_2} \left[(\mathbf{E}_o^-)_z (\mathbf{E}_o^+)_x [q_o^+ (q_o^+ \cos \phi - K \sin \phi) + \hat{q}_o^- D_1] - \right. \\ &\quad \left. - (\mathbf{E}_o^-)_x (\mathbf{E}_o^+)_z [q_o^+ (q_o^+ \cos \phi + K \sin \phi) + \hat{q}_o^- D_1] + \right. \\ &\quad \left. + (\mathbf{E}_o^+)_y B_2 + (\mathbf{E}_o^-)_y B_3 \right] \\ t_{os} &= \frac{(\mathbf{E}_e^+)_x q_e^+ r_{oe} - (\mathbf{E}_o^-)_x q_o^+ + (\mathbf{E}_o^+)_x q_o^+ r_{oo}}{\hat{q}_o^-} \\ t_{op} &= -\frac{(\mathbf{E}_o^-)_z q_o^+ - (\mathbf{E}_o^-)_y K - B_4 r_{oe} - B_5 r_{oo}}{D_1} \end{aligned} \quad (33)$$

and for an extraordinary incident wave:

$$\begin{aligned} r_{eo} &= \frac{1}{N_2} \left[(\mathbf{E}_e^-)_x (q_e^- - \hat{q}_o^-) [D_2 + (\mathbf{E}_e^+)_y K \cos \phi] + \right. \\ &\quad \left. + (\mathbf{E}_e^+)_x (\hat{q}_o^- - q_e^+) [D_3 + (\mathbf{E}_e^-)_y K \cos \phi] \right] \end{aligned}$$

$$\begin{aligned} r_{ee} &= -\frac{1}{N_2} \left[(\mathbf{E}_e^-)_x (q_e^- - \hat{q}_o^-) D_4 - (\mathbf{E}_e^-)_x (\mathbf{E}_o^+)_y K \cos \phi (\hat{q}_o^- - q_e^-) + \right. \\ &\quad \left. + (\mathbf{E}_e^-)_y B_3 + (\mathbf{E}_o^+)_x (\hat{q}_o^- - q_o^+) D_3 \right] \\ t_{es} &= \frac{(\mathbf{E}_e^-)_x q_e^- + (\mathbf{E}_e^+)_x q_e^+ r_{ee} + (\mathbf{E}_o^+)_x q_o^+ r_{eo}}{\hat{q}_o^-} \\ t_{ep} &= -\frac{(\mathbf{E}_e^-)_z + (\mathbf{E}_e^+)_z r_{ee} + (\mathbf{E}_o^+)_z r_{eo}}{\cos \phi} \end{aligned} \quad (34)$$

where ϕ is the exitant angle and

$$\begin{aligned} B_1 &= -(\mathbf{E}_e^+)_x K \cos \phi (\hat{q}_o^- - q_e^+) & B_2 &= -(\mathbf{E}_o^-)_x K \cos \phi (\hat{q}_o^- + q_o^+) \\ B_3 &= -(\mathbf{E}_o^+)_x K \cos \phi (\hat{q}_o^- - \hat{q}_o^-) & B_4 &= (\mathbf{E}_e^+)_y K + (\mathbf{E}_e^+)_z q_e^+ \\ B_5 &= (\mathbf{E}_o^+)_y K + (\mathbf{E}_o^+)_z q_o^+ \\ D_1 &= K \sin \phi - \hat{q}_o^- \cos \phi & D_2 &= (\mathbf{E}_e^+)_z (D_1 + q_e^+ \cos \phi) \\ D_3 &= (\mathbf{E}_e^-)_z (D_1 + q_e^- \cos \phi) & D_4 &= (\mathbf{E}_o^+)_z (D_1 + q_o^+ \cos \phi) \end{aligned}$$

and the normalization factor is

$$\begin{aligned} N_2 &= (\mathbf{E}_e^+)_x (q_e^+ - \hat{q}_o^-) D_4 + \\ &\quad + (\mathbf{E}_o^+)_x (\hat{q}_o^- - q_o^+) D_2 + (\mathbf{E}_o^+)_y B_1 + (\mathbf{E}_e^+)_y B_3 \end{aligned}$$

Anisotropic-to-Anisotropic Boundary

Solving the full system results in rather complicated coefficients. Due to their length those coefficients are unfortunately usually omitted from literature. In our supplemental material we provide the equations in the form of MATLAB scripts.

Appendix B: Optical Path Differences

In this appendix we list the OPDs used in section 4 using the same notation. The OPDs used in D_0 (equation 13) are the OPDs of the order 0 ordinary and extraordinary path:

$$\begin{aligned} \Delta \mathcal{P}_o^\downarrow &= d \left(\frac{\eta_o + (I_o)_z K'}{|(I_o)_y|} - \mathcal{P}_o \right) \equiv 0 \\ \Delta \mathcal{P}_e^\downarrow &= d \left(\frac{\eta_{ef} + (I_e)_z K'}{|(I_e)_y|} - \mathcal{P}_o \right) \end{aligned} \quad (35)$$

where $\mathcal{P}_o = \frac{\eta_o + (I_o)_z K'}{|(I_o)_y|}$.

The operator \mathcal{D} is then

$$\begin{aligned} \mathcal{D} &= \mathcal{D}^\downarrow \mathcal{D}^\uparrow = \\ &\begin{bmatrix} \hat{r}_{oo} r_{oo} e^{ik\Delta \mathcal{P}_{oo}} + \hat{r}_{oe} r_{eo} e^{ik\Delta \mathcal{P}_{eo}} & \hat{r}_{oo} r_{oe} e^{ik\Delta \mathcal{P}_{oe}} + \hat{r}_{oe} r_{ee} e^{ik\Delta \mathcal{P}_{ee}} \\ \hat{r}_{eo} r_{oo} e^{ik\Delta \mathcal{P}_{oo}} + \hat{r}_{ee} r_{eo} e^{ik\Delta \mathcal{P}_{eo}} & \hat{r}_{eo} r_{oe} e^{ik\Delta \mathcal{P}_{oe}} + \hat{r}_{ee} r_{ee} e^{ik\Delta \mathcal{P}_{ee}} \end{bmatrix} \end{aligned} \quad (36)$$

where the OPDs are essentially the OPDs of the order 1 paths that start at the lower interface:

$$\begin{aligned} \Delta \mathcal{P}_{oo} &= \Delta \mathcal{P}_o^\downarrow + \Delta \mathcal{P}_o^\uparrow = d \left(\frac{\eta_o + (I_o)_z K'}{|(I_o)_y|} + \frac{\eta_o + (\hat{I}_o)_z K'}{|(\hat{I}_o)_y|} - 2\mathcal{P}_o \right) \\ \Delta \mathcal{P}_{eo} &= \Delta \mathcal{P}_o^\downarrow + \Delta \mathcal{P}_e^\uparrow = d \left(\frac{\eta_o + (I_o)_z K'}{|(I_o)_y|} + \frac{\hat{\eta}_{ef} + (\hat{I}_e)_z K'}{|(\hat{I}_e)_y|} - 2\mathcal{P}_o \right) \\ \Delta \mathcal{P}_{oe} &= \Delta \mathcal{P}_e^\downarrow + \Delta \mathcal{P}_o^\uparrow = d \left(\frac{\eta_{ef} + (I_e)_z K'}{|(I_e)_y|} + \frac{\eta_o + (\hat{I}_o)_z K'}{|(\hat{I}_o)_y|} - 2\mathcal{P}_o \right) \end{aligned}$$

$$\Delta\mathcal{P}_{ee} = \Delta\mathcal{P}_e^\downarrow + \Delta\mathcal{P}_e^\uparrow = d \left(\frac{\eta_{ef} + (\hat{I}_e)_z K'}{|(\hat{I}_e)_y|} + \frac{\hat{\eta}_{ef} + (\hat{I}_e)_z K'}{|(\hat{I}_e)_y|} - 2\mathcal{P}_o \right) \quad (37)$$

where $K' = \eta_i \sin \theta$. The first subscript denotes the type of ray taken from the lower interface to the upper interface and the second subscript denotes the type of ray taken downwards after reflection off the upper interface.

Appendix C: Derivation of the Spectral Integral

In this appendix we derive the expression for the spectral integral used in equation 19. Using the same notation as in section 5 we first write $J_n = (\mathcal{J}_n)_s = \sum_p^{2n+1} E_p e^{i\Delta\phi_p}$ where E_p are real scalar amplitudes which are independent of the wavelength. Using Euler's formula the spectral integral $\mathbf{S} = \mathcal{S}(|\mathcal{J}_s|^2, \Lambda) = \mathcal{S}(|\sum_n J_n|^2, \Lambda)$ then becomes

$$\mathbf{S} = \int_\lambda \Lambda(\lambda) \left[\left(\sum_j E_j \cos(\Delta\phi_j) \right)^2 + \left(\sum_j E_j \sin(\Delta\phi_j) \right)^2 \right] d\lambda \quad (38)$$

Expanding each squared term and using the trigonometric identity $\cos(\theta + \phi) = \cos\theta\cos\phi - \sin\theta\sin\phi$ to group the resulting cosine and sine terms leads to

$$\mathbf{S} = \int_\lambda \Lambda(\lambda) \left[\sum_j E_j^2 + 2 \sum_{j < q} E_j E_q \cos(\Delta\phi_j - \Delta\phi_q) \right] d\lambda \quad (39)$$

Finally we use the fact that Λ is normalized and that the scalar electric field amplitudes are independent of λ by assumption and we also rewrite the inner sum as an iteration over the order differences between the phase shifts:

$$\begin{aligned} \mathbf{S} &= \sum_j E_j^2 + 2 \sum_j \sum_{l=1}^{\infty} E_j E_{j+l} \int_\lambda \Lambda(\lambda) \cos(\Delta\phi_j - \Delta\phi_{j+l}) d\lambda = \\ &= \mathcal{E} + 2\mathcal{H} \end{aligned} \quad (40)$$